Surface Biology and Geology (SBG)

Level-3 Evapotranspiration L3 (JET) Algorithm Theoretical Basis Document

Simon Hook, Kerry Cawse-Nicholson, Gregory Halverson, Brenna Hatch, Maggie Johnson, Madeleine Pascolini-Campbell, AJ Purdy, Munish Sikka, Claire Villanueva-Weeks

SBG Science Team
Jet Propulsion Laboratory
California Institute of Technology

Contacts

Readers seeking additional information about this document may contact the following SBG Science Team members:

- Kerry Cawse-Nicholson
  Mailstop 183-601
  Jet Propulsion Laboratory
  4800 Oak Grove Dr.
  Pasadena, CA 91109
  Email: kerry-anne.cawse-nicholson@jpl.nasa.gov
  Office: (818) 354-1594

- Gregory Halverson
  Mailstop 233-300
  Jet Propulsion Laboratory
  4800 Oak Grove Dr.
  Pasadena, CA 91109
  Email: gregory.h.halverson@jpl.nasa.gov
  Office: (626) 660-6818 (Mobile)

- Simon J. Hook
  MS 183-600
  Jet Propulsion Laboratory
  4800 Oak Grove Dr.
  Pasadena, CA 91109
  Email: simon.j.hook@jpl.nasa.gov
  Office: (818) 354-0974

List of Acronyms

ALEXI	Atmosphere–Land Exchange Inverse
ATBD	Algorithm Theoretical Basis Document
Cal/Val	Calibration and Validation
CONUS	Contiguous United States
ECOSTRESS	ECOsystem Spaceborne Thermal Radiometer Experiment on Space Station
ET	Evapotranspiration
ESI	Evaporative Stress Index
EVI-2	Earth Ventures Instruments, Second call
FLiES	Forest Light Environmental Simulator
GEO	Group on Earth Observations
GEWEX	Global Energy and Water Cycle Exchanges Project
GLEAM	Global Land-surface Evaporation: the Amsterdam Methodology
GMAO	Global Modeling and Assimilation Office
HyspIRI	Hyperspectral Infrared Imager
IGBP	International Geosphere-Biosphere Program
iLEAPs	International Land Ecosystem-Atmospheric Processes Study
ISS	International Space Station
L-2	Level 2
L-3	Level 3
LE	Latent heat flux
LST	Land Surface Temperature
MERRA	Modern Era Retrospective-Analysis for Research and Applications
METRIC	Mapping EvapoTranspiration at high-Resolution with Internalized Calibration
MODIS	MODerate-resolution Imaging Spectroradiometer
MPI-BGC	Max Planck Institute for Biogeochemistry
NSE	Nash-Sutcliffe Efficiency
PHyTIR	Prototype HyspIRI Thermal Infrared Radiometer
PM-MOD16	Penman-Monteith MOD16
PMBL	Penman-Monteith-Bouchet-Lhomme
PT-JPL	Priestley-Taylor Jet Propulsion Laboratory
RMSD	Root Mean Squared Difference
SBG	Surface Biology and Geology
SDS	Science Data System
SEBS	Surface Energy Balance System
STIC	Surface Temperature Initiated Closure
TIR	Thermal Infrared
VIC	Variable Infiltration Capacity
VIIRS	Visible Infrared Imaging Radiometer Suite
WUE	Water Use Efficiency

Contents

1 Introduction

1.1 Purpose

Evapotranspiration (ET) is one of the main science outputs from the Surface Biology and Geology (SBG). ET is a Level-3 (L-3) product constructed from a combination of the SBG Level-2 (L-2) Land Surface Temperature (LST) product and ancillary data sources. The rate of ET is controlled by many environmental and biological controls including: incoming radiation, the atmospheric water vapor deficit, soil water availability, and vegetation physiology and phenology (Brutsaert, 1982; Monteith, 1965; Penman, 1948). Therefore, to accurately model ET, it remains important to consider these variables. Scientists have been able to form models that ingest satellite observations that capture environmental and biological controls on ET across the globe. Because LST holds the unique ability to capture when and where plants experience stress, as observed by elevated temperatures, LST can inform which areas have a reduced capacity to evaporate or transpire water to the atmosphere (Allen et al., 2007). In this Algorithm Theoretical Basis Document (ATBD), we describe the Jet Propulsion Laboratory ET (JET) Ensemble approach taken to resolve ET globally is the heritage from the ECOSTRESS mission that we consider as a set of candidate algorithms for SBG..

1.2 Scope and Objectives

In this ATBD, we provide:

1. Description of the ET parameter characteristics and requirements;
2. Description of the general form of the ET algorithms in the JET ensemble;
3. Required algorithm-specific adaptations specific to the SBG mission;
4. Required Ancillary data products with potential sources and back-up sources;
5. Plan for the calibration and validation (Cal/Val) of the ET retrieval.

2 Parameter Description and Requirements

Attributes of the ET data produced by the SBG mission include:

- Spatial resolution of 60 m x 60 m;

- Diurnally varying temporal resolution to match the overpass characteristics of the International Space Station (ISS);

- Latency as required by the SBG Science Data System (SDS) processing system;

- Ancillary Variables

Ancillary variable	Equation	Source
Albedo (α)	STARS	**Harmonized Landsat Sentinel (HLS) 2.0 product; Suomi NPP Visible Infrared Imaging Radiometer Suite (VIIRS) VNP09GA product**
Normalized difference vegetation index (NDVI)	STARS	**SBG ASI VNIR camera; Harmonized Landsat Sentinel (HLS) 2.0 product; Suomi NPP Visible Infrared Imaging Radiometer Suite (VIIRS) VNP09GA product**
Near-surface air temperature (T_a)	L3G MET	**GEOS-5 FP tavg1_2d_slv_Nx product**
Near surface dew point temperature (T_d)	Net radiation	**GEOS-5 FP tavg1_2d_slv_Nx product**
Relative humidity (RH)	L3G MET	**GEOS-5 FP tavg1_2d_slv_Nx product**
Soil moisture (SM)	L3G SM product	**GEOS-5 FP tavg1_2d_lnd_Nx product**

Table 1. Showing ancillary variables and their respective equations, and data sources.

3.1 STARS NDVI and Albedo

SBG produces coincident, gap-filled NDVI and albedo estimates at 60 m SBG standard resolution for each daytime SBG overpass through multi-instrument fusion of ancillary VSWIR data from high spatial resolution instruments (Sentinel 2A/B, Landsat, SBG) and moderate spatial but high temporal resolution instruments (Suomi NPP Visible Infrared Imaging Radiometer Suite (VIIRS)). Specific instrument data products considered for NDVI and albedo are described in Table 2.

	NDVI	Albedo (α)
High (<100 m) spatial	Harmonized Landsat Sentinel 2.0 (30 m, 3-5 day) SBG ASI VNIR (60m, coincident)	Harmonized Landsat Sentinel 2.0 (30m, 3-5 day) SBG VSWIR (30m, 16 day)
High (daily) temporal	VIIRS VNP09GA (500 m)	VIIRS VNP09GA (1km)

Table 2. Data sources for STARS fusion of NDVI and albedo.

Prior to data fusion, a pixelwise, lagged 16-day implementation of the VNP43 algorithm (Schaaf, 2017) is used for a near-real-time bi-directional reflectance function (BRDF) correction on the VNP09GA reflectance products to produce VIIRS nadir BRDF-adjusted red and near-infrared reflectance at 500 m resolution for NDVI, and 1 km estimates of black-sky albedo (a_{black}) and white-sky albedo (a_{white}) for VIIRS M-bands 1, 2, 3, 4, 5, 7, 8, 10, and 11. Blue-sky albedo (a_{white}) for each of these bands is calculated as in (Schaaf, 2017)

$$a_{blue} = SKYL \cdot a_{white} + (1 - SKYL)a_{black}$$

where SKYL is the fraction of diffuse skylight read from a look-up table according to solar zenith angle and aerosol optical depth (AOD) retrieved from GEOS-5 FP tavg3_2d_aer_Nx. The broadband blue-sky albedo is calculated by a weighted sum of the VIIRS M-band blue-sky albedo estimates using the near-to-broadband coefficients described in (Schaaf, 2017) described in Table 3.

VIIRS M-Band	NTB Coefficient
1	0.2418
2	-0.201
3	0.2093
4	0.1146
5	0.1146
7	0.1348
8	0.2251
10	0.1123
11	0.0860
Offset	-0.0131

Table 3. Near-to-Broadband (NTB) coefficients for VIIRS M-band albedo (Schaaf, 2017).

A near-to-broadband albedo is estimated from the Harmonized Landsat Sentinel (HLS) products using the Sentinel-2a/b coefficients in Table 4 and Landsat 8 coefficients in Table 5. The 30 m albedo estimates from HLS are up-sampled to the 60m SBG standard resolution prior to data fusion.

Band	NTB Coefficient
2	0.1324
3	0.1269
4	0.1051
5	0.0971
6	0.0890
7	0.0818
8	0.0722
11	0.0167
Offset	0.0002

Table 4. Near-to-Broadband (NTB) coefficients for Sentinel-2a/b albedo (Vanino, 2018).

Landsat 8 Band	NTB Coefficient
2	0.356
3	0.13
4	0.373
5	0.085
6	0.072
Offset	-0.018

Table 5. Near-to-Broadband coefficients for Landsat 8 albedo (Liang, 2001).

The data fusion is performed using a variant of the Spatial Timeseries for Automated high-Resolution multi-Sensor data fusion (STARS) methodology (Johnson et al., 2022). STARS is a statistical, state-space timeseries methodology that provides streaming data fusion and uncertainty quantification through efficient Kalman filtering. For SBG, the STARS method is implemented for NDVI and albedo, separately, as follows. Let $x_{i,t}$ represent NDVI/albedo to be estimated in the ith 60 m SBG resolution pixel on day t. Let $Y_{i,t}^f$ represent measurements from the high spatial resolution instruments at the ith 60 m pixel. Note that $Y_{i,t}^c$ is assumed to be missing if there is no high spatial resolution overpasses on day t. Then, let $Y_{j,t}^c$ represent the coarse spatial resolution VIIRS measurement at the jth cell in the VIIRS resolution grid ($\approx$500 m for NDVI, $\approx$1 km for albedo) and let A_j be the set of all 60m pixels overlapped by the VIIRS pixel. The statistical model for SBG STARS has the following form

$$Y_{j,t}^c = \frac{1}{|A_j|} \sum_{i \in A_j} x_{i,t} + \epsilon_{j,t}^c \qquad \epsilon_{j,t}^c \sim Normal(0, \sigma_c^2) \qquad (1a)$$

$$Y_{i,t}^f = x_{i,t} + \epsilon_{i,t}^f \qquad \epsilon_{j,t}^f \sim Normal(0, \sigma_f^2) \qquad (1b)$$

$$x_{i,t} = x_{i,t-1} + \omega_{i,t} \qquad \omega_{i,t} \sim GP(0, \tau^2, \mathcal{K}(\cdot)) \qquad (2)$$

where equations (1a,b) describe the instrument measurements as noisy, aggregate in the case of VIIRS, observations of the target high resolution image values, $x_{i,t}$. Measurement errors are assumed to be mean-zero and normally distributed with standard deviations σ_c, σ_f for coarse and fine instruments, respectively. Equation 2 describes day-to-day temporal dependence in NDVI/albedo through a first-order Markov chain where the magnitudes of pixel-level changes between days ($\omega_{i,t}$) follow a Gaussian process (GP) with covariance function $\mathcal{K}(\cdot)$, modelling spatial correlation of day-to-day changes between pixels. The standard deviation parameter, τ, constrains the expected magnitude of change. To achieve scalability, STARS is implemented in a block, moving window where blocks are defined by the coarse resolution grid plus a spatial buffer region.

For $x_t = (\dots, x_{i,t}, \dots)$ the vector of the n target image pixels within a block on day t, and y_t the stacked vector of available coarse and fine measurements, the timeseries model above induces the full state space model

$$y_t = F_t x_t + \epsilon_t \qquad\qquad \epsilon_t \sim MultivariateNormal(0, V) \qquad\qquad (3)$$
$$x_t = x_{t-1} + \omega_t \qquad\qquad \omega_t \sim MultivariateNormal(0, W) \qquad\qquad (4)$$

where V is a diagonal matrix with elements σ_f^2, σ_c^2. The matrix, F_t, is the aggregation matrix analog to the linking of coarse and fine measurements to the target resolution grid in equation (1a,b). The estimation of the target 60m NDVI/albedo images on day t is inferred through the posterior distribution of x_t given all considered past and current measurements up to day t. This distribution is known to be Gaussian with mean, m_t, and covariance, C_t. The mean provides the estimated imagery, while the covariance provides quantified uncertainties characterizing uncertainty due to spatial and temporal downscaling. Estimates of m_t and C_t are obtained recursively through the well-known Kalman filtering equations (Kalman, 1960). Specifically, given estimates of m_t, C_t, and any new observations on day $t + 1$ (y_{t+1}), the updated estimates of m_{t+1}, and C_{t+1} are calculated as

$$m_{t+1} = m_t + K_{t+1}(y_{t+1} - F_{t+1}m_t) \qquad\qquad (5)$$

$$C_{t+1} = (I - K_{t+1}F_{t+1})(C_t + W) \qquad\qquad (6)$$

where $K_{t+1} = (C_t + W)F_{t+1}^T(F_{t+1}(C_t + W)F_{t+1}^T + V)^{-1}$ is the Kalman gain matrix. If neither no new measurements are available on day $t + 1$, the mean estimate is propagated forward ($m_{t+1} = m_t$) but the covariance is increased ($C_{t+1} = C_t + W$) quantifying increased uncertainty in fused estimates due to lack of available data. By leveraging a timeseries approach to data fusion, STARS provides automated spatial and temporal gapfilling, uncertainty quantification, and the capability to provide estimates of coincident albedo with any SBG overpass. These pixel-wise uncertainties of the NDVI and albedo estimates are distributed as data layers in the STARS product.

Near-real-time STARS NDVI/albedo products corresponding to each daytime L2T_LSTE product are produced by loading the set of means and covariances produced for the day of the previous L2T_LSTE product, downloading any available measurements (VIIRS, HLS, etc.) between overpasses, and Kalman filtering forward the NDVI/albedo estimates to the current target day. The latency of this operation depends on the latency of the products in Table 1. The coincident STARS NDVI and albedo products are recorded in the L2T_STARS product.

3.2 Downscaled Meteorology and Soil Moisture
Near-surface air temperature (Ta) and relative humidity (RH) are sourced from the GEOS-5 FP tavg1_2d_slv_Nx product. Soil moisture (SM) is sourced from the GEOS-5 FP tavg1_2d_lnd_Nx product.

The Ta, RH, and SM inputs of the ET models are retrieved at low latency from the GEOS-5 FP dataset at coarse resolution, approximately a third of a degree. To improve the spatial fidelity of evapotranspiration processing, these coarse meteorological estimates are spatially downscaled to

9

the fine spatial structure of the SBG surface temperature and STARS albedo. Future versions of this product will include a more robust method.

The ST, NDVI, and albedo are spatially aggregated to the GEOS-5 FP spatial resolution. A linear regression is calculated from these three variables as independent variables to the GEOS-5 FP variable as the dependent variable for each of the GEOS-5 FP variables. The coefficients from this regression are applied to the fine resolution SBG surface temperature and STARS albedo to produce a fine resolution estimate of air temperature, humidity, or soil moisture. This fine scale estimate is bias corrected by spatially aggregating to the GEOS-5 FP scale, measuring the bias against the GEOS-5 FP estimate, and spatially interpolating this coarse scale bias to the 60 m SBG grid, and subtracting this interpolated bias. Cloud-obstructed areas of are filled in with bi-cubically resampled GEOS-5 FP. The meteorology variables Ta and RH are recorded in the L3T MET and mosaicked into the L3G MET. The SM data is recorded in the L3T SM product and mosaicked into the L3G SM product.

3.3 Net Radiation

The generation of net radiation (R_n) involves the integrated retrieval of individual radiation balance components: downwelling shortwave radiation (R_{SD}), upwelling shortwave radiation (R_{SU}), downwelling longwave radiation (R_{LD}), and upwelling longwave radiation (R_{LU}) [*Verma et. al,* 2016]:

$$R_N = (R_{SD} - R_{SU}) + (R_{LD} - R_{LU}) \tag{7}$$

where *a* is the surface albedo.

NETRAD	Equations	Data Variable & Sources
R_{SD}	FLiES	Cloud Optical Thickness and Aerosol Optical Thickness (GEOS-5 FP)
R_{SU}	$R_{SU} = \alpha R_{SD}$	Land Surface Albedo (STARS)
R_{LD}	$R_{LD} = \sigma \varepsilon_A T_a^4$	Near Surface Air Temperature and Vapor Pressure (GEOS-5 FP)
R_{LU}	$R_{LU} = \sigma \varepsilon_S T_S^4$	Land Surface Temperature and Emissivity (ECO2LSTE)

Table 2. Showing radiation balance components and their respective equations, variables, and data sources

R_{SD} is calculated from an atmospheric radiative transfer model, the Forest Light Environmental Simulator (FLiES) [*Iwabuchi*, 2006; *Kobayashi and Iwabuchi*, 2008; *Ryu et al.*, 2011; *Ryu et al.*, 2012]. To speed processing, a neural network machine learning algorithm was trained on to generate R_{SD} from solar zenith angle, aerosol optical thickness, cloud optical thickness, land surface albedo, atmospheric profile height, aerosol type, and cloud height. R_{SU} is calculated from R_{SD} and land surface albedo () as:

$$R_{SU} = \alpha R_{SD} \tag{8}$$

R_{LD} is calculated from Stefan-Boltzmann's Law:

$$R_{LD} = \sigma \varepsilon_A T_a^4 \tag{9}$$

$$\varepsilon_A = 1 - \left(1 + .467 \frac{Ea}{Ta}\right) \backslash aste^{-\sqrt{1.2 + 3\frac{4.65 \cdot E_a}{T_a}}} \tag{10}$$

$$E_A = 2.171 * 10^{\left(10*e^{-\frac{4157}{Td} - 33.91}\right)} \tag{11}$$

where σ is the Stefan-Boltzmann constant (5.67x10^{-8} W m^{-2} K^{-4}), ε_A is the atmospheric emissivity calculated from total atmospheric precipitable water (ζ) [*Prata*, 1996], T_a is near surface air temperature, Ea is the vapor pressure, and T_d is the near surface dew point temperature. T_a and T_d (°C) are available from GEOS-5 [*Verma et. al,* 2016]:

R_{LU} is calculated from Stefan-Boltzmann's Law [*Verma et. al,* 2016]:

$$R_{LU} = \sigma \varepsilon_S T_S^4 \tag{12}$$

where ε_S is the broadband surface emissivity and T_S is surface temperature available from the SBG LST_LSTE product.

We emphasize these data products provide data at unprecedented scales. Therefore, we solicit feedback on the quality and utility of these variables in their ability to advance science and scientific applications. A preliminary evaluation of the ancillary data accuracy is presented in Section 5.

4 Evapotranspiration Retrieval: Jet Propulsion Laboratory EvapoTranspiration (JET) Ensemble

The JPL EvapoTranspiration (JET) data ensemble provides a robust estimation of ET from multiple ET models. The JET ensemble incorporates ET data from four algorithms: Priestley Taylor-Jet Propulsion Laboratory model with soil moisture (PT-JPL$_{SM}$), the Penman Monteith MODIS Global Evapotranspiration Model (MOD16), Soil Temperature Initiated Closure (STIC) model, and the Breathing Earth System Simulator (BESS) model. We present descriptions of these models here, inherited from the ECOSTRESS mission, as candidates for SBG L3 evapotranspiration processing.

4.1 PT-JPL$_{SM}$: General Form

The PT-JPL$_{SM}$ model relies on the Priestley-Taylor [1972] equation to resolve potential ET (PET). This formulation is removed from the need to parameterize stomatal and aerodynamic resistances and instead multiples the α coefficient (1.26) to the rate of equilibrium ET:

$$(13)$$

$$PT = \alpha \frac{\Delta}{\Delta + \gamma} R_N - G$$

where Δ is the slope of the saturation-to-vapor pressure curve (dependent on near surface air temperature, T_a, and atmospheric vapor pressure, e_a), γ is the psychrometric constant, and R_N is net radiation (W m^{-2}) and G is the ground heat flux (W m^{-2}). *PET* is given in units of R_N, or W m^{-2}, and is therefore considered as an energy variable, i.e., LE. To convert LE to ET, one can divide *LE* by the latent heat of vaporization (MJ kg^{-1}).

To reduce PET to actual ET (AET), *Fisher et al.* [2008] applied ecophysiological constraint functions (*f*-functions, unitless multipliers, 0-1) based on atmospheric moisture (vapor pressure deficit, VPD; and, RH) and vegetation indices (normalized difference and soil adjusted vegetation indices, NDVI and SAVI, respectively). While this model has been demonstrated to perform well at large scales in space and time, certain model assumptions of land-atmosphere equilibrium fall apart at finer spatial and temporal frequencies. As a result, the PT-JPL formulation from *Fisher et al.* [2008] has been shown to overestimate ET in arid regions. To overcome these limitations *Purdy et al.* [2018] modified the algorithm to incorporate explicit constraint from soil water availability. The driving equations in the PT-JPL$_{SM}$ algorithm are:

$$AET = ET_s + ET_c + ET_i \tag{14}$$

$$ET_s = \left(f_{wet} + f_{rew}(1 - f_{wet})\right)\alpha \frac{\Delta}{\Delta + \gamma}(R_{ns} - G) \tag{15}$$

$$(16)$$

$$ET_C = (1 - f_{wet})f_{trm}f_g f_t \alpha \frac{\Delta}{\Delta + \gamma} R_{nc}$$

$$(17)$$

$$ET_i = f_{wet}\alpha \frac{\Delta}{\Delta + \gamma} R_{nc}$$

where ET_s, ET_c, and ET_i are evaporation from the soil, canopy and intercepted water, respectively, each calculated explicitly and summing to total *AET*. f_{wet} is relative surface wetness (RH^4) [*Stone et al.*, 1977] representing the fraction of soil and canopy that delivers water to the atmosphere potential rate. f_{rew} is the relative extractable water defined as the difference between observed soil moisture (θ_{obs}) and soil moisture at the plant wilting point (θ_{wp}) divided by the difference of soil moisture at field capacity (θ_{fc}) and soil moisture at the plant wilting point ($\frac{\theta_{obs} - \theta_{wp}}{\theta_{fc} - \theta_{wp}}$). Canopy constraints include the fraction of green canopy ($f_g = f_{APAR}/f_{IPAR}$) [*Zhang et al.*,

2005], plant temperature constraints ($f_t = \exp(-((T_{max}-T_{opt})/T_{opt})^2)$) [*Potter et al.*, 1993; *June et al.*, 2004], and plant and soil moisture controls (f_{trm}) [*Purdy et al.*, 2018]. f_{APAR} is absorbed photosynthetically active radiation (PAR), f_{IPAR} is intercepted PAR, T_{max} is maximum air temperature, T_{opt} is T_{max} at $\max(R_n T_{max} \frac{SAVI}{VPD})$, G is the soil heat flux, and R_{nc}, R_{ns} are the net radiation ('c' for canopy and 's' for soil). f_{trm} combines both f_m the plant moisture control and soil moisture control on transpiration (f_{trew}) by weighting each constraint by the relative humidity as:

$$f_{trm} = \left(RH^{4(1-VWC)(1-RH)}\right)f_m + \left(1 - RH^{4(1-VWC)(1-RH)}\right)f_{trew} \tag{18}$$

During periods of high humidity, plant moisture is a stronger control than soil water control. During periods of low humidity, soil water control is greater (Figure 1).
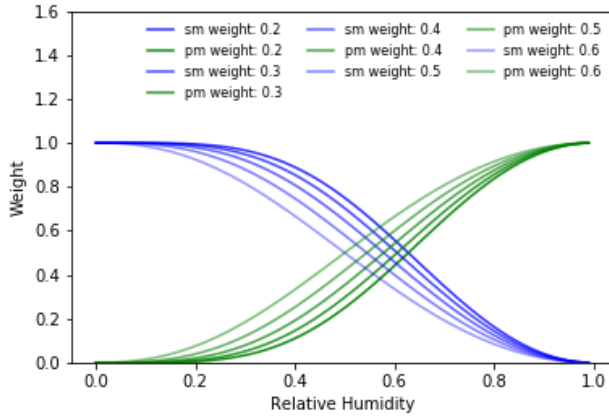

Figure 1) Plant moisture (green) and soil water control (blue) weight by relative humidity (x-axis) and VWC (legend values: 0.2-0.6). During periods of high relative humidity periods higher weights on plant moisture indicate more control from this scalar. During low humidity more weight is placed on soil water control.

The individual plant moisture and soil water constraints on transpiration are derived as:

$$ \tag{19}$$

$$f_m = \frac{f_{APAR}}{f_{APARmax}}$$

$$ \tag{20}$$

$$f_{trew} = 1 - \left(\frac{\theta_{cr} - \theta_{obs}}{\theta_{cr} - \theta_{wpch}}\right)^{CH_{scalar}}$$

where CH_{scalar} is a canopy height scalar that impacts the sensitivity of vegetation to soil water availability equal to $\sqrt{CH}$ and capped between 1 and 5, θ_{cr} is the critical soil moisture at which soil water availability begins to constrain ET and computed as:

$$\theta_{cr} = \left(1 - \left(\frac{1}{1+PET} - 0.1\frac{1}{1+CH}\right)\right)\left(\theta_{fc} - \frac{\theta_{WP}}{CH_{scalar}}\right) + \frac{\theta_{WP}}{CH_{scalar}} \tag{21}$$

The adjustment of θ_{fc} to θ_{cr} is removed from the dependence on land classification datasets and facilitates continuously mapping when soil water availability begins to limit transpiration within f_{trew} (Figure 2).
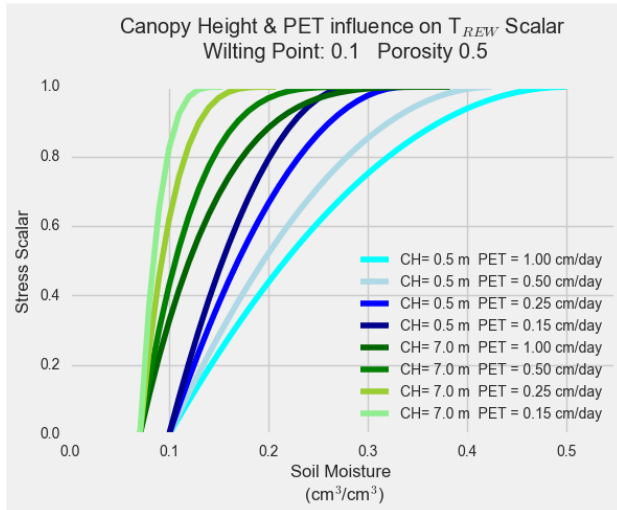

Figure 2) Supplemental figure from Purdy et al., 2018. *f_{trew}* on canopy height and PET (see legend). During high PET conditions soil water control begins sooner than during low PET conditions. Canopy height impacts when soil water control begins with taller canopies (greens) being less sensitive to surface soil water control than shorter canopies (blues).

1   Spatial resolution improvements

To maintain continuity with other SBG data products, ET from PT-JPL$_{SM}$ is produced at 60 m. This required generating ancillary variables such as NDVI, albedo (α), air temperature (Ta), relative humidity (RH), soil moisture (SM), canopy height, and soil properties at the same spatial resolution. Section 3 details how NDVI, albedo, air temperature, relative humidity, soil moisture, and net radiation were resampled or downscaled to fill this need. Soil properties and canopy height data were sourced from X and Y. We advise caution to users interested in highly heterogeneous land surfaces and meteorological conditions at length scales less than 1 km.

4.2   STIC: General Form

The Surface Temperature Initiated Closure (STIC) (latest version 1.3) is a one-dimensional SEB model treating soil-vegetation as a single unit [*Mallick et al., 2015; 2018; 2022*]. STIC directly integrates LST into the Penman-Monteith Shuttleworth-Wallace system of ET equations [*Penman, 1965; Shuttleworth and Wallace, 1985*] to solve the aerodynamic temperature, which is the most critical temperature for ET modeling. STIC assumes a first-order dependence of aerodynamic conductance (g_a) and canopy conductance (g_{cs}) on LST (through soil moisture availability and aerodynamic temperature (T_0)). Surface moisture availability (also called surface wetness) is first estimated as a function of LST, and then constrains g_a and g_{cs} conductances through the surface wetness in an analytical framework. In addition to LST, the inputs to

STIC1.3 include radiation (net radiation), emissivity, albedo, fractional vegetation cover (FVC) (derived from NDVI), and meteorological inputs (air temperature, relative humidity, and incoming solar radiation).

The general approach to STIC is (and see flow diagram in Figure 1):

> (1) STIC solves the state equations to find analytical solution of T_0, and the conductances (g_a and g_{cs}).
> (2) There are more unknowns in the state equations (e.g., aerodynamic vapor pressure components), these unknowns are initialized as a function of LST.
> (3) The additional unknowns are estimated iteratively by combining Penman-Monteith and Shuttleworth-Wallace equations

The state equations solved in Step 1 are as follows:

$$F_E = \frac{2\alpha s}{2s + 2\gamma + \gamma(1 + I_{SM})\frac{g_a}{g_{cs}}}$$

(22)

$$T_0 = T_a + \frac{(e_0 - e_a)}{\gamma}\frac{(1 - F_E)}{F_E}$$

(23)

$$g_a = \frac{R_N - G}{\rho c_p \left[(T_0 - T_a) + \frac{(e_0 - e_a)}{\gamma}\right]}$$

(24)

$$g_{cs} = g_a \frac{(e_0 - e_a)}{(e_0^* - e_0)}$$

(25)

Where F_E is the evaporative fraction (defined as the fractional contribution of ET from total available energy), α is the Priestley-Taylor coefficient [*Priestley & Taylor, 1972*], s is the slope of the saturation vapor pressure at air temperature (T_a) (hPa/°C), γ is the psychrometric constant (hPa/°C), e_0^* and e_0 are the saturation vapor pressure and ambient vapor pressure at the canopy-air stream, also called source-sink height (hPa), R_N and G are net radiation and ground heat flux (W/m²), e_a is the atmospheric vapor pressure (hPa) at the level of T_a measurement, ρ is the air density (kg/m³), and c_p is the specific heat of air at constant pressure (j/kg/K).

I_{SM} describes the relative wetness or the intensity of water stress on a surface. This variable controls the transition from potential to actual evaporation, with I_{SM} tending to 1 on a unstressed wet surface, and 0 on a stressed dry surface. Since LST is extremely sensitive to surface water stress variations, it is used directly to estimate I_{SM}. For further details, refer to Mallick et al. [*2018, 2022*].

In Step 1, initial estimates of an initial estimate of e_0^*, e_0, I_{SM}, and surface dew point temperature (T_{sd}), are obtained. The initial I_{SM} and R_N are used for an initial estimate of G. In Step 2, initial estimates of the conductances, T_0, F_E and sensible heat (H) and latent heat flux (LE) are obtained. In Step 3, the process is iterated by updating e_0^*, e_0, I_{SM}, and α, and used to recalculate G, g_a, g_{cs}, T_0, F_E, H, and LE until convergence of LE is obtained (10 – 15 iterations).

The major differences of version 1.3 [*Mallick et al.,* 2022] from the previous version concern the calculation of G, which is calculated according to Santanello and Friedl [*2003*] with the following function:

$$\frac{G}{R_N} = c_g \left[\frac{2\pi(t_{g0} + 10800)}{t_g} \right]$$

(26)

Where c_g is the maximum proportion of G/R_N; t_{g0} is time in seconds relative to solar noon, t_g is the factor that minimizes the deviation between G/R_N and governs the phase difference between G and R_N. c_g and t_g are linked to surface wetness I_{SM} with:

(27)

$$c_g = (1 - I_{SM})c_{gmax} + I_{SM}c_{gmin}$$

(28)

$$t_g = (1 - I_{SM})t_{gmax} + I_{SM}t_{gmin}$$

Using the values of c_{gmax} (0.35), c_{gmin} (0.05), t_{gmax} (100000 s), and t_{gmin}(74000 s). With the initial estimate of I_{SM}, initial G is estimated, and then updated in the iterative process. Further details are available in the supporting information of [*Mallick et al. 2022*].

For its implementation in SBG, we modified the STIC version 1.3 equation in the following ways:

- We use a different method to calculate dew point temperature (T_d) with relative humidity (RH) and air temperature (T_a):

$$T_d = T_a - ((100 - RH * 100) / 5)$$

- The inputs R_N , albedo, emissivity, NDVI, relative humidity, air temperature and incoming solar radiation are the same as used for other models in the JET ensemble. This is done in order to have more consistency in the input data.

4.3   MOD16: General Form

The MOD16 algorithm is rooted in the Penman Monteith equation with environmental constraints from vegetation cover, temperature, and atmospheric moisture deficits (Mu et al.,

2011). Similar to the PT-JPLSM model, the MOD16 algorithm resolves evaporative fluxes from the soil, canopy, and intercepted water separately.

$$AET = ET_s + ET_c + ET_i \tag{29}$$

$$ET_S = \left(f_{wet} + (1 - f_{wet})RH^{\frac{e_{sat}-e}{\beta}}\right) \frac{sA_C + \frac{\rho Cp(e_{sat} - e)}{r_{a_s}}}{\Delta + \gamma\left(1 + \frac{r_{S_s}}{r_{a_s}}\right)} \tag{30}$$

$$ET_S = (1 - f_{wet})f_c \frac{sA_C + \frac{\rho Cp(e_{sat} - e)}{r_{a_s}}}{\Delta + \gamma\left(1 + \frac{r_{S_s}}{r_{a_s}}\right)} \tag{31}$$

$$ET_S = f_{wet}f_c \frac{sA_C + \frac{\rho Cp(e_{sat} - e)}{r_{a_s}}}{\Delta + \gamma\left(1 + \frac{r_{S_s}}{r_{a_s}}\right)} \tag{32}$$

Where f_{wet} is fraction of wet surface, RH is the relative humidity, s is the slope of saturated water vapor pressure to temperature ($d(e_{sat})/dT$); A is the available energy with subscripts to distinguish differences between the soil and canopy; ρ is the air density; Cp is the specific heat capacity of air; γ is the psychromatic constant; e is the actual water vapor pressure; r_a is the aerodynamic resistance; and r_s is the surface resistance. Vegetation-dependent environmental constraints on stomatal conductance are incorporated through the surface resistance in the formulation above.

4.4 BESS: General Form

BESS is a coupled biophysical modeling system that couples atmospheric and canopy radiative transfer processes with photosynthesis, stomatal conductance, and transpiration using (Ryu et al., 2011). BESS applies an equilibrium evaporation representation to resolve soil evaporation and solves a quadratic representation of the Penman Monteith model to estimate transpiration [*Jiang et. al*, 2016]:

$$AET = ET_s + ET_c \tag{33}$$

$$ET_s = \frac{s}{(s + \gamma)}(R_{ns} - G)RH^{VPD} \tag{34}$$

$$aET_c^2 + bET_c + c = 0 \tag{35}$$

$$a = \frac{r_a^2}{2[\rho_a C_p \gamma(r_a + r_c)]} \frac{d^2 e_{sat}(T_a)}{dT_a^2} \tag{36}$$

$$b = -1 - r_a \frac{d e_{sat}(T_a)}{d(T_a)} \frac{1}{\gamma(r_a + r_c)} - \frac{R_{nj} r_a^2}{\rho_a C_p \gamma(r_a + r_c)} \frac{d^2 e_{sat}(T_a)}{dT_a^2} \tag{37}$$

$$\tag{38}$$

$$c = \frac{\rho_a C_p D}{\gamma(r_a + r_c)} + \frac{r_a R_{nj}}{\gamma(r_a + r_c)} \frac{d e_{sat}(T_a)}{dT_a} + \frac{1}{2} \frac{(r_a R_{nj})^2}{\rho_a C_p \gamma(r_a + r_c)} \frac{d^2 e_{sat}(T_a)}{dT_a^2}$$

where r_a is the aerodynamic; r_c is the canopy resistance; R_{nj} is the net radiation; ρ_a is the air density; γ is the psychrometric constant; $e_{sat}(T_a)$ is the saturated water vapor pressure at temperature T_a.

4.5 Daily Ensemble Value

Differences in model structure provide a range in ET estimates to consider for each 70m pixel. Previous studies have shown the combination of an ensemble of modeled values provides improved or equal accuracy to any one given model [Kirtman et al., 2014]. Due to the limited number of models used within the JET algorithm, we adopt a simplified approach by taking the median value of the instantaneous ET ensemble (PT-JPL$_{SM}$, MOD16, STIC, TSEB, & BESS). The ensemble median value is used to provide a daily estimate of ET for each 60 m pixel. Additionally, the uncertainty is estimated as the standard deviation of the ensemble for each pixel.

5 Calibration/Validation

5.1 ET evaluation

To evaluate remote sensing ET datasets requires ground observations at similar length scales and temporal frequencies. Eddy covariance (EC) towers provide year-round observations at frequencies (~30 minutes) and spatial scales (10's-100's m) that capture exchanges of water vapor from the land surface to the atmosphere necessary to evaluate the JET ensemble. Here, we employ EC observations from the Ameriflux network due to their data collection standards, availability, and distribution across various land uses in North and South America. We only include EC towers in our analysis that are within SBG observations (<58ºN & > 58ºS), have data during SBG mission (2018-Present), and have a long-term closure ration of greater than 0.70. This filtering resulted in 74 towers across 11 land uses for the JET ensemble comparison (Figure X).
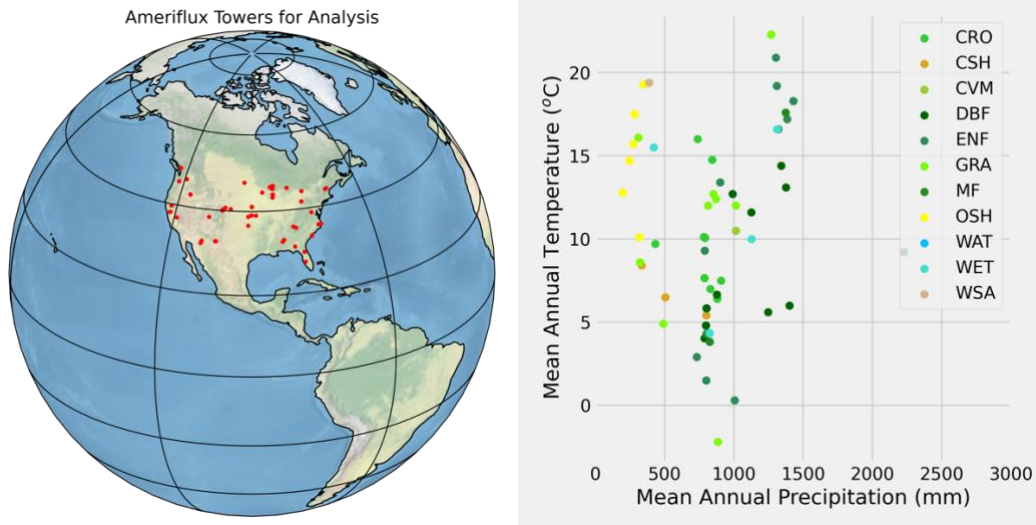
Figure X) Left: Distribution of filtered Ameriflux towers across North America within SBG view. Right: Range in EC towers' mean annual precipitation (x-axis), temperature (y-axis) by vegetation class (color).

EC data from Ameriflux are post-processed for quality and to ensure surface energy budget closure. Surface energy balance variables including sensible heat, latent heat, ground heat flux, and net radiation were filtered for outliers according to a median of absolute deviation about the median approach [Papale et al., 2006]. Next, the surface energy budget was closed while preserving the Bowen Ratio, the ratio of sensible heat to latent heat, following the EBC_CF Method 1 and EBC_CF Method 2 procedures of the OneFLUX processing [Pastorello et al., 2020]. This closure approach yields energy closures according to the 25th, 50th, and 75th percentiles for dates spanning plus or minus 15 and 5 days respectively. Only cloud-free SBG observations are utilized in this analysis. Due to uncertainties and on-going debate about the surface energy imbalances from EC observations, we compute the statistics computed based on the best comparison across the raw observation and the closed budget options. We compute statistics of unbiased root mean square error, mean absolute bias, and the correlation coefficient.

Error Budget
The SBG ET products will target an error value of 1 mm per day with an estimated 0.1 mm of this attributed to instrument error. This target is consistent with established literature and validation work on the related PT-JPL ET, DisALEXI-JPL ET, MOD16 and MYD16 ET products in recent years. Fisher et al. (2019) found that the RMSE of PT-JPL instantaneous ET was 6%, with $R^2 = 0.88$, (overall RMSE was 41.3 W/m2 compared to a mean of 182.0 W/m2 and a range of 713.8 W/m2). An examination of the error propagation of PT-JPL ET from Halverson et al. finds that ET products exhibited strong responses to changes in vegetation and temperature; consistent with previous findings on DisALEXI-JPL ET which established that LST error within 1K enables ET estimates to be accurate to within 1mm/day (Cawse-Nicholson et al., 2020). In 2021, Cawse-Nicholson et. al, evaluated DisALEXI-JPL daily ET and found an RMSE of 0.81 mm/day. Mu et al. found that MOD16 and MYD16 exhibited an RMSE of 0.84 mm/day.

5.2 WUE Evaluation

BESS uses a carbon-water-coupled model to separately evaluate C3 and C4 species provided by a global map [Still, 2013 10.1029/2001GB001807] for a given pixel, the sum of that relative proportion of C3 and C4 in that pixel determines the GPP [Jiang et al., 2016]. The GPP product in kilograms of carbon per square meter estimated by BESS is ingested operationally into the data production stream to estimate water use efficiency (WUE). Process-based approaches like BESS have an advantage to represent the interaction between the soil system, plants, and atmosphere as an organic integration rather than ingesting GPP semi-empirically [Jiang et al., 2016]. The carbon uptake is divided by the daily ET in kilograms per square meter to determine the ratio of grams of carbon fixed to kilograms of water lost in units of ET. This ratio describes the WUE, higher values indicate more plant productivity, lower values indicate less productive plants.

$$(39)$$

$$WUE = \frac{GPP}{ET}$$

5.3 ESI Evaluation

The Evaporative Stress Index (ESI) is used as a climate indicator of agricultural drought and plant stress by comparison of ET to PET to determine anomalous reduction in ET relative to potential ET. PET is already calculated internally in the PT-JPL algorithm and can be used directly to compute the ESI without ancillary information.

$$(29)$$

$$ESI = \frac{ET}{PET}$$

5.4 Ancillary variable evaluation

EC towers commonly measure Ta, RH, and SM in addition to capturing exchanges of radiative energy, carbon, and water from the Earth's surface and atmosphere. We utilize the same Ameriflux data source. Instead of screening for surface energy balance closure, we only consider the quality of each variable when considering data for use in this evaluation. For soil moisture, we only utilize EC towers data from the National Ecological Observation Network (NEON) due to the number of soil moisture observations. Recently, the NEON towers provided a great comparison to evaluate the utility of remotely sensed soil moisture in forested and non-forested regions [Ayres et al., 2022]. For each variable we compute statistics of unbiased root mean square error, mean absolute bias, and the correlation coefficient.

6 Mask/Flag Derivation

For T_s and e_s, the ECOSTRESS L2 flags are used to provide quality information for the L3 ET product.

7   Metadata

- unit of measurement: Watts per square meter (W m^{-2})
- range of measurement: 0 to 3000 W m^{-2}
- projection: SBG swath
- spatial resolution: 60 m x 60 m
- temporal resolution: dynamically varying with precessing ISS overpass; instantaneous throughout the day, local time
- spatial extent: all land globally, excluding poleward ±60°
- start date time: near real-time
- end data time: near real-time
- number of bands: not applicable
- data type: float
- min value: 0
- max value: 3000
- no data value: 9999
- bad data values: 9999
- flags: quality level 1-4 (best to worst)

8   Acknowledgements

We thank Gregory Halverson, Laura Jewell, Gregory Moore, Caroline Famiglietti, Munish Sikka, Manish Verma, Kevin Tu, Alexandre Guillaume, Kaniska Mallick, Youngryel Ryu, and Hideki Kobayashi for contributions to the algorithm development described in this ATBD.

9 References

Allen, R. G., M. Tasumi, and R. Trezza (2007), Satellite-based energy balance for mapping evapotranspiration with internalized calibration (METRIC)-model, *J. Irrig. Drain. E.*, *133*, 380-394. doi: https://doi.org/10.1061/(ASCE)0733-9437(2007)133:4(380)

Anderson, M. C., J. M. Norman, J. R. Mecikalski, J. A. Otkin, and W. P. Kustas (2007), A climatological study of evapotranspiration and moisture stress across the continental United States based on thermal remote sensing: 1. Model formulation, *J. Geophys. Res.*, *112*(D10), D10117. doi: https://doi.org/10.1029/2006JD007506

Anderson, M. C., W. P. Kustas, C. R. Hain, C. Cammalleri, F. Gao, M. Yilmaz, I. Mladenova, J. Otkin, M. Schull, and R. Houborg (2013), Mapping surface fluxes and moisture conditions from field to global scales using ALEXI/DisALEXI, *Remote Sensing of Energy Fluxes and Soil Moisture Content*, 207-232. doi: https://doi.org/10.3390/rs13040773

Baldocchi, D. (2008), 'Breathing' of the terrestrial biosphere: lessons learned from a global network of carbon dioxide flux measurement systems, *Australian Journal of Botany*, *56*, 1-26. doi: https://doi.org/10.1071/BT07151

Baldocchi, D., E. Falge, L. H. Gu, R. J. Olson, D. Hollinger, S. W. Running, P. M. Anthoni, C. Bernhofer, K. Davis, R. Evans, J. Fuentes, A. Goldstein, G. Katul, B. E. Law, X. H. Lee, Y. Malhi, T. Meyers, W. Munger, W. Oechel, K. T. P. U, K. Pilegaard, H. P. Schmid, R. Valentini, S. Verma, T. Vesala, K. Wilson, and S. C. Wofsy (2001), FLUXNET: A new tool to study the temporal and spatial variability of ecosystem-scale carbon dioxide, water vapor, and energy flux densities, *Bulletin of the American Meteorological Society*, *82*(11), 2415-2434. doi: https://doi.org/10.1175/1520-0477(2001)082<2415:FANTTS>2.3.CO;2

Bi, L., P. Yang, G. W. Kattawar, Y.-X. Hu, and B. A. Baum (2011), Diffraction and external reflection by dielectric faceted particles, *J. Quant. Spectrosc. Radiant. Transfer*, *112*, 163-173. doi: https://doi.org/10.1016/j.jqsrt.2010.02.007

Bisht, G., V. Venturini, S. Islam, and L. Jiang (2005), Estimation of the net radiation using MODIS (Moderate Resolution Imaging Spectroradiometer), *Remote Sensing of Environment*, *97*, 52-67.doi: https://doi.org/10.1016/j.rse.2005.03.014

Bouchet, R. J. (1963), Evapotranspiration re´elle evapotranspiration potentielle, signification climatique*Rep. Publ. 62*, 134-142 pp, Int. Assoc. Sci. Hydrol., Berkeley, California. doi:

Chen, X., H. Wei, P. Yang, and B. A. Baum (2011), An efficient method for computing atmospheric radiances in clear-sky and cloudy conditions, *J. Quant. Spectrosc. Radiant. Transfer*, *112*, 109-118. doi: https://doi.org/10.1016/j.jqsrt.2010.08.013

Chen, Y., J. Xia, S. Liang, J. Feng, J. B. Fisher, X. Li, X. Li, S. Liu, Z. Ma, and A. Miyata (2014), Comparison of satellite-based evapotranspiration models over terrestrial ecosystems in China, *Remote Sensing of Environment*, *140*, 279-293. doi: https://doi.org/10.1016/j.rse.2013.08.045

Coll, C., Z. Wan, and J. M. Galve (2009), Temperature-based and radiance-based validations of the V5 MODIS land surface temperature product, *Journal of Geophysical Research*, *114*(D20102), doi: https://doi.org/10.1029/2009JD012038.

Ershadi, A., M. F. McCabe, J. P. Evans, N. W. Chaney, and E. F. Wood (2014), Multi-site evaluation of terrestrial evaporation models using FLUXNET data, *Agricultural and Forest Meteorology*, *187*, 46-61. doi: https://doi.org/10.1016/j.agrformet.2013.11.008

Famiglietti, C. A., J. B. Fisher, G. Halverson, and E. E. Borbas (2018), Global validation of MODIS near-surface air and dew point temperatures, *Geophysical Research Letters*, *45*, 1-9. doi: https://doi.org/10.1029/2018GL077813

Fisher, J. B., K. Tu, and D. D. Baldocchi (2008), Global estimates of the land-atmosphere water flux based on monthly AVHRR and ISLSCP-II data, validated at 16 FLUXNET sites, *Remote Sensing of Environment*, *112*(3), 901-919. doi: https://doi.org/10.1016/j.rse.2007.06.025

Fisher, J. B., R. H. Whittaker, and Y. Malhi (2011), ET Come Home: A critical evaluation of the use of evapotranspiration in geographical ecology, *Global Ecology and Biogeography*, *20*, 1-18. doi: https://doi.org/10.1111/j.1466-8238.2010.00578.

Fisher, J. B., D. D. Baldocchi, L. Misson, T. E. Dawson, and A. H. Goldstein (2007), What the towers don't see at night: Nocturnal sap flow in trees and shrubs at two AmeriFlux sites in California, *Tree Physiology*, *27*(4), 597-610. doi: https://doi.org/10.1093/treephys/27.4.597

Fisher, J. B., S. Hook, R. Allen, M. Anderson, A. French, C. Hain, G. Hulley, and E. Wood (2014), The ECOsystem Spaceborne Thermal Radiometer Experiment on Space Station (ECOSTRESS): science motivation, paper presented at American Geophysical Union Fall Meeting, San Francisco.

Fisher, J. B., F. Melton, E. Middleton, C. Hain, M. Anderson, R. Allen, M. F. McCabe, S. Hook, D. Baldocchi, P. A. Townsend, A. Kilic, K. Tu, D. D. Miralles, J. Perret, J.-P. Lagouarde, D. Waliser, A. J. Purdy, A. French, D. Schimel, J. S. Famiglietti, G. Stephens, and E. F. Wood (2017), The future of evapotranspiration: Global requirements for ecosystem functioning, carbon and climate feedbacks, agricultural management, and water resources, *Water Resources Research*, *53*, 2618-2626. doi: https://doi.org/10.1002/2016WR020175

Fisher, J. B., Y. Malhi, A. C. de Araújo, D. Bonal, M. Gamo, M. L. Goulden, T. Hirano, A. Huete, H. Kondo, T. Kumagai, H. W. Loescher, S. Miller, A. D. Nobre, Y. Nouvellon, S. F. Oberbauer, S. Panuthai, C. von Randow, H. R. da Rocha, O. Roupsard, S. Saleska, K. Tanaka, N. Tanaka, and K. P. Tu (2009), The land-atmosphere water flux in the tropics, *Global Change Biology*, *15*, 2694-2714. doi: https://doi.org/10.1111/j.1365-2486.2008.01813.x

García, M., I. Sandholt, P. Ceccato, M. Ridler, E. Mougin, L. Kergoat, L. Morillas, F. Timouk, R. Fensholt, and F. Domingo (2013), Actual evapotranspiration in drylands derived from in-situ and satellite data: Assessing biophysical constraints, *Remote Sensing of Environment*, *131*, 103-118. doi: https://doi.org/10.1016/j.rse.2012.12.016

Goulden, M. L., J. W. Munger, S. M. Fan, B. C. Daube, and S. C. Wofsy (1996), Measurements of carbon sequestration by long-term eddy covariance: methods and a critical evaluation of accuracy, *Global Change Biology*, *2*, 169-182. doi: https://doi.org/10.1111/j.1365-2486.1996.tb00070.x

Halverson, G., M. Barker, S. Cooley, and S. Pestana (2016), Costa Rica agriculture: applying ECOSTRESS diurnal cycle land surface temperature and evapotranspiration to agricultural soil and water management*Rep.*

Iqbal, M. (2012), *An introduction to solar radiation*, Elsevier.

Iwabuchi, H. (2006), Efficient Monte Carlo Methods for Radiative Transfer Modeling, *Journal of the Atmospheric Sciences*, *63*(9), 2324-2339. doi: https://doi.org/10.1175/JAS3755.1

June, T., J. R. Evans, and G. D. Farquhar (2004), A simple new equation for the reversible temperature dependence of photosynthetic electron transport: a study on soybean leaf, *Functional Plant Biology*, *31*(3), 275-283. doi: https://doi.org/10.1071/FP03250

Jung, M., M. Reichstein, and A. Bondeau (2009), Towards global empirical upscaling of FLUXNET eddy covariance observations: validation of a model tree ensemble approach

using a biosphere model, *Biogeosciences*, *6*, 2001-2013. doi: https://doi.org/10.5194/bg-6-2001-2009

Kirtman, B. P., Min, D., Infanti, J. M., Kinter, J. L., III, Paolino, D. A., Zhang, Q., van den Dool, H., Saha, S., Mendez, M. P., Becker, E., Peng, P., Tripp, P., Huang, J., DeWitt, D. G., Tippett, M. K., Barnston, A. G., Li, S., Rosati, A., Schubert, S. D., Rienecker, M., Suarez, M., Li, Z. E., Marshak, J., Lim, Y., Tribbia, J., Pegion, K., Merryfield, W. J., Denis, B., & Wood, E. F. (2014). The North American Multimodel Ensemble: Phase-1 Seasonal-to-Interannual Prediction; Phase-2 toward Developing Intraseasonal Prediction, *Bulletin of the American Meteorological Society*, *95*(4), 585-601. doi: https://doi.org/10.1175/BAMS-D-12-00050.1

Kobayashi, H., and H. Iwabuchi (2008), A coupled 1-D atmosphere and 3-D canopy radiative transfer model for canopy reflectance, light environment, and photosynthesis simulation in a heterogeneous landscape, *Remote Sensing of Environment*, *112*(1), 173-185. doi: 10.1016/j.rse.2007.04.010

Lagouarde, J., and Y. Brunet (1993), A simple model for estimating the daily upward longwave surface radiation flux from NOAA-AVHRR data, *International Journal of Remote Sensing*, *14*(5), 907-925. doi: https://doi.org/10.1080/01431169308904386

Liang, X., D. P. Lettenmaier, E. Wood, and S. J. Burges (1994), A simple hydrologically based model of land surface water and energy fluxes for general circulation models, *Journal of Geophysical Research*, *99*(D7), 14415-14428. doi: https://doi.org/10.1029/94JD00483

Mallick, K., A. Jarvis, J. B. Fisher, K. P. Tu, E. Boegh, and D. Niyogi (2013), Latent heat flux and canopy conductance based on Penman-Monteith, Priestley-Taylor equation, and Bouchet's complementary hypothesis, *Journal of Hydrometeorology*, *14*, 419-442. doi: https://doi.org/10.1175/JHM-D-12-0117.1

Mallick, K., A. J. Jarvis, E. Boegh, J. B. Fisher, D. T. Drewry, K. P. Tu, S. J. Hook, G. Hulley, J. Ardö, and J. Beringer (2014), A Surface Temperature Initiated Closure (STIC) for surface energy balance fluxes, *Remote Sensing of Environment*, *141*, 243-261. doi: https://doi.org/10.1016/j.rse.2013.10.022

Mallick, K., Boegh, E., Trebs, I., Alfieri, J. G., Kustas, W. P., Prueger, J. H., ... & Jarvis, A. J. (2015). Reintroducing radiometric surface temperature into the P enman-M onteith formulation. *Water Resources Research*, *51*(8), 6214-6243. doi: https://doi.org/10.1002/2014WR016106

Mallick, K., Toivonen, E., Trebs, I., Boegh, E., Cleverly, J., Eamus, D., ... & Garcia, M. (2018). Bridging Thermal Infrared Sensing and Physically-Based Evapotranspiration Modeling: From Theoretical Implementation to Validation Across an Aridity Gradient in Australian Ecosystems. *Water Resources Research*, *54*(5), 3409-3435. doi: https://doi.org/10.1029/2017WR021357

Mallick, K., Baldocchi, D., Jarvis, A., Hu, T., Trebs, I., Sulis, M., ... & Kustas, W. P. (2022). Insights Into the Aerodynamic Versus Radiometric Surface Temperature Debate in Thermal-Based Evaporation Modeling. *Geophysical Research Letters*, *49*(15), e2021GL097568. doi: https://doi.org/10.1029/2021GL097568

McCabe, M. F., A. Ershadi, C. Jimenez, D. G. Miralles, D. Michel, and E. F. Wood (2016), The GEWEX LandFlux project: evaluation of model evaporation using tower-based and globally gridded forcing data, *Geosci. Model Dev.*, *9*(1), 283-305. doi: https://doi.org/10.5194/gmd-9-283-2016

Michel, D., C. Jiménez, D. Miralles, M. Jung, M. Hirschi, A. Ershadi, B. Martens, M. McCabe, J. Fisher, and Q. Mu (2016), TheWACMOS-ET project–Part 1: Tower-scale evaluation of four remote-sensing-based evapotranspiration algorithms, *Hydrology and Earth System Sciences*, *20*(2), 803-822. doi: https://doi.org/10.3929/ethz-a-010611421

Miralles, D., C. Jiménez, M. Jung, D. Michel, A. Ershadi, M. McCabe, M. Hirschi, B. Martens, A. Dolman, and J. Fisher (2016), The WACMOS-ET project, part 2: evaluation of global terrestrial evaporation data sets, *Hydrology and Earth System Sciences*, *20*(2), 823-842. doi: https://doi.org/10.5194/hess-20-823-2016

Miralles, D. G., T. R. H. Holmes, R. A. M. De Jeu, J. H. Gash, A. G. C. A. Meesters, and A. J. Dolman (2011), Global land-surface evaporation estimated from satellite-based observations, *Hydrol. Earth Syst. Sci.*, *15*(2), 453-469. doi: https://doi.org/10.5194/hess-15-453-2011

Monteith, J. L. (1965), Evaporation and the environment, *Symposium of the Society of Exploratory Biology*, *19*, 205-234.

Mu, Q., M. Zhao, and S. W. Running (2011), Improvements to a MODIS global terrestrial evapotranspiration algorithm, *Remote Sensing of Environment*, *111*, 519-536. doi: https://doi.org/10.1016/j.rse.2011.02.01

Papale, D., and A. Valentini (2003), A new assessment of European forests carbon exchange by eddy fluxes and artificial neural network spatialization, *Global Change Biology*, *9*, 525-535. doi: https://doi.org/10.1046/j.1365-2486.2003.00609.x

Papale, D., Reichstein, M., Aubinet, M., Canfora, E., Bernhofer, C., Kutsch, W., Longdoz, B., Rambal, S., Valentini, R., Vesala, T., and Yakir, D.: Towards a standardized processing of Net Ecosystem Exchange measured with eddy covariance technique: algorithms and uncertainty estimation, Biogeosciences, 3, 571–583. doi: https://doi.org/10.5194/bg-3-571-2006

Pastorello, G., Trotta, C., Canfora, E. *et al.* The FLUXNET2015 dataset and the ONEFlux processing pipeline for eddy covariance data. *Sci Data* **7**, 225 (2020). doi: https://doi.org/10.1038/s41597-020-0534-3

Penman, H. L. (1948), Natural evaporation from open water, bare soil and grass, *Proceedings of the Royal Society of London Series A*, *193*, 120-146. doi: https://doi.org/10.1098/rspa.1948.0037

Potter, C. S., J. T. Randerson, C. B. Field, P. A. Matson, P. M. Vitousek, H. A. Mooney, and S. A. Klooster (1993), Terrestrial ecosystem production: a process based model based on global satellite and surface data, *Global Biogeochemical Cycles*, *7*(4), 811-841. doi: https://doi.org/10.1029/93gb02725

Prata, A. J. (1996), A new long-wave formula for estimating downward clear-sky radiation at the surface, *Quarterly Journal of the Royal Meteorological Society*, *122*(533), 1127-1151. doi: https://doi.org/10.1002/qj.49712253306

Price, J. C. (1977), Thermal inertia mapping: a new view of the earth, *Journal of Geophysical Research*, *82*(18), 2582-2590. doi: https://doi.org/10.1029/JC082i018p02582

Priestley, C. H. B., and R. J. Taylor (1972), On the assessment of surface heat flux and evaporation using large scale parameters, *Monthly Weather Review*, *100*, 81-92. doi: https://doi.org/10.1175/1520-0493(1972)100<0081:OTAOSH>2.3.CO;2

Roesch, A., C. Schaaf, and F. Gao (2004), Use of Moderate-Resolution Imaging Spectroradiometer bidirectional reflectance distribution function products to enhance simulated surface albedos, *Journal of Geophysical Research*, *109*(D12), doi: 10.1029/2004JD004552.

Ryu, Y., D. D. Baldocchi, H. Kobayashi, C. van Ingen, J. Li, T. A. Black, J. Beringer, E. van Gorsel, A. Knohl, B. E. Law, and O. Roupsard (2011), Integration of MODIS land and atmosphere products with a coupled-process model to estimate gross primary productivity and evapotranspiration from 1 km to global scales, *Global Biogeochem. Cycles*, *25*(4), GB4017. doi: https://doi.org/10.1029/2011GB004053

Ryu, Y., D. D. Baldocchi, T. A. Black, M. Detto, B. E. Law, R. Leuning, A. Miyata, M. Reichstein, R. Vargas, C. Ammann, J. Beringer, L. B. Flanagan, L. Gu, L. B. Hutley, J. Kim, H. McCaughey, E. J. Moors, S. Rambal, and T. Vesala (2012), On the temporal upscaling of evapotranspiration from instantaneous remote sensing measurements to 8-day mean daily-sums, *Agricultural and Forest Meteorology*, *152*(0), 212-222. doi: 10.1016/j.agrformet.2011.09.010

Santanello Jr, J. A., & Friedl, M. A. (2003). Diurnal covariation in soil heat flux and net radiation. *Journal of Applied Meteorology*, *42*(6), 851-862. doi: https://doi.org/10.1175/1520-0450(2003)042<0851:DCISHF>2.0.CO;2

Shuttleworth, W. J., & Wallace, J. (1985). Evaporation from sparse crops-an energy combination theory. *Quarterly Journal of the Royal Meteorological Society*, **111**, 839–855. doi: https://doi.org/10.1002/qj.49711146910

Stone, P. H., S. Chow, and W. J. Quirr (1977), July climate and a comparison of January and July climates simulated by GISS general circulation model, *Monthly Weather Review*, *105*(2), 170-194. doi: https://doi.org/10.1175/1520-0493(1977)105<0170:TJCAAC>2.0.CO;2

Su, Z. (2002), The Surface Energy Balance System (SEBS) for estimation of turbulent heat fluxes, *Hydrology and Earth System Sciences*, *6*, 85-99. doi: https://doi.org/10.5194/hess-6-85-2002

Vinukollu, R. K., E. F. Wood, C. R. Ferguson, and J. B. Fisher (2011), Global estimates of evapotranspiration for climate studies using multi-sensor remote sensing data: Evaluation of three process-based approaches, *Remote Sensing of Environment*, *115*, 801-823. doi: https://doi.org/10.1016/j.rse.2010.11.006

Wang, K., P. Wang, Z. Li, M. Cribb, and M. Sparrow (2007), A simple method to estimate actual evapotranspiration from a combination of net radiation, vegetation index, and temperature, *Journal of Geophysical Research*, *112*(D15107), doi:10.1029/2006JD008351. doi: Wang, K., P. Wang, Z. Li, M. Cribb, and M. Sparrow (2007), A simple method to estimate actual evapotranspiration from a combination of net radiation, vegetation index, and temperature, Journal of Geophysical Research, 112(D15107), doi:10.1029/2006JD008351.

Wind, G., S. Platnick, M. D. King, P. A. Hubanks, M. J. Pavolonis, A. K. Heidinger, P. Yang, and B. A. Baum (2010), Multilayer cloud detection with the MODIS near-infrared water vapor absorption band, *Journal of Applied Meteorology and Climatology*, *49*, 2315-2333. doi: https://doi.org/10.1175/2010JAMC2364.1

Yang, F., M. A. White, A. R. Michaelis, K. Ichii, H. Hashimoto, P. Votava, A.-X. Zhu, and R. R. Nemani (2006), Prediction of continental-scale evapotranspiration by combining MODIS and AmeriFlux data through support vector machine, *Geoscience and Remote Sensing, IEEE Transactions on*, *44*(11), 3452-3461. doi: https://doi.org/10.1109/TGRS.2006.876297

Zhang, L., B. Wylie, T. Loveland, E. Fosnight, L. L. Tieszen, L. Ji, and T. Gilmanov (2007), Evaluation and comparison of gross primary production estimates for the Northern Great Plains grasslands, *Remote Sensing of Environment*, *106*(2), 173-189. doi: https://doi.org/10.1016/j.rse.2006.08.012

Zhang, Q., X. Xiao, B. H. Braswell, E. Linder, J. Aber, and B. Moore (2005), Estimating seasonal dynamics of biophysical and biochemical parameters in a deciduous forest using MODIS data and a radiative transfer model, *Remote Sensing of Environment*, *99*, 357-371. doi: https://doi.org/10.1016/j.rse.2005.09.009